ADVANCED MATERIALS
www.advmat.de

Dual Roles of Deep Eutectic Solvent in Polysulfide Redox and Catalysis for Intermediate-Temperature Potassium-Sulfur Batteries

Liying Tian, Qian Wu, Kai Tang, Zhiqiang Tang, Zhenghao Yang, Zihan Shen, Longcheng Zhang, Wen Xie, Yuan Yang, and Zhichuan J. Xu**

Potassium–sulfur (K-S) batteries hold great promise for long-duration energy storage due to their low cost and high energy density. However, the irreversible deposition of K_2S_2/K_2S severely hinders sulfur utilization and cycling stability. Herein, a NiS–DES interfacial regulation strategy is developed that leverages the dual functionality of a deep eutectic solvent (DES) to govern the adsorption and conversion behavior of K_2S_2/K_2S at the catalytic interface, enabling their highly reversible transformation. Specifically, DES forms moderate electronic coupling with NiS to weaken the excessively strong adsorption of K_2S and prevent catalyst deactivation. Simultaneously, strong electronic interactions between DES and K_2S promote interfacial activation and conversion, thereby extending the reaction pathway and enhancing reduction depth. As a result, the intermediate-temperature K-S batteries deliver an initial capacity of 810 mAh g^{-1} with a minimal capacity decay of 0.02%/cycle over 1300 cycles at 6 mg cm^{-2} sulfur loading. Even under lean catholyte (4.2 µL $mg_{[sulfur]}^{-1}$) and higher sulfur loading (12 mg cm^{-2}), they achieve 521 mAh g^{-1} initially, retaining stability with 0.03%/cycle decay over 500 cycles. This NiS-30DES system achieves a cell-level energy density exceeding 150 Wh kg^{-1} and a low levelized cost of storage (LCOS) of $140/MWh, demonstrating strong potential for scalable long-duration energy storage.

1. Introduction

The global energy transition is accelerating the decarbonization of the energy sector.[1] The long-duration energy storage (LDES) technologies play a crucial role in mitigating the intermittency of renewable energy.[2,3] By enabling energy transfer across extended timescales, these systems are essential for reducing dependence on fossil fuels.[4] However, limited cycle life and low cumulative cycle counts increase storage costs.[5] For example, LDES may operate ≈1500 cycles for weekly use and ≈400 cycles for monthly use over 30 years, far fewer than ≈10 000 cycles typical of short-term storage with daily cycling.[6] These challenges underscore the need for advancements in cycle life and efficiency, driving research into alternative battery chemistries and designs.[7,8]

Sodium-sulfur (Na-S) batteries are widely regarded as the most promising long-duration energy storage systems (LDES), owing to the abundance and low cost of sodium and sulfur.[9–11] High-temperature (HT) Na-S batteries with β''-alumina solid electrolytes (BASE) and molten sodium and sulfur as electrodes have been successfully commercialized (**Figure 1a**).[12,13] But they typically operate at high temperatures of 300–350 °C, which poses significant safety concerns, increases maintenance costs, and reduces reliability. In light of these challenges, recent research has focused on lowering the operating temperature and developing safer Na-S batteries that can function at intermediate temperature (IT) or room temperature (RT).[11,14]

RT Na-S batteries possess high energy density but face challenges such as sulfur electrode expansion, shuttle effects, and dendrite growth, leading to low reversible capacity and rapid degradation (Figure 1b).[15,16] In contrast, IT Na-S batteries (below 150 °C) are receiving increasing attention because they take advantage of their HT and RT counterparts. IT Na-S batteries use BASE and molten alkali metal anodes, effectively preventing polysulfide shuttling and suppressing dendrite growth.[17] Additionally, organic electrolytes in the cathode, such as tetraglyme (TEGDME), accelerate reaction kinetics and mitigate volume expansion (Figure 1c).[9]

L. Tian, Q. Wu, K. Tang, Z. Shen, L. Zhang, W. Xie, Z. J. Xu
School of Material Science and Engineering
Nanyang Technological University
50 Nanyang Avenue, Singapore 639798, Singapore
E-mail: xuzc@ntu.edu.sg

Z. Tang
Singapore-MIT Alliance for Research and Technology Center
M3S IRG 1 CREATE Way, #09-03 CREATE Tower, Singapore 138602, Singapore

Z. Yang, Y. Yang
Department of Applied Physics and Applied Mathematics
Columbia University
New York, NY 10027, USA
E-mail: yy2664@columbia.edu

The ORCID identification number(s) for the author(s) of this article can be found under https://doi.org/10.1002/adma.202507114

DOI: 10.1002/adma.202507114

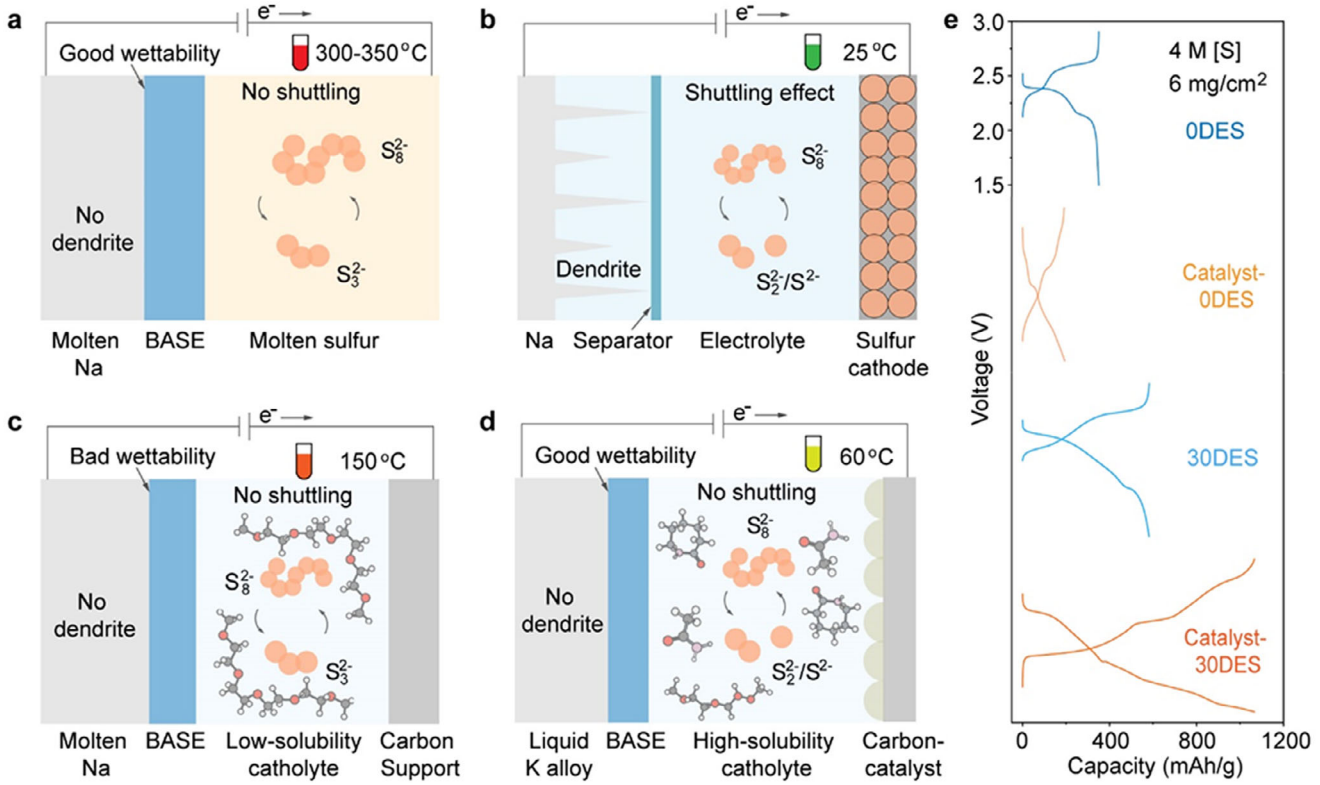

Figure 1. Configuration and Reaction Process of Na-S and K-S Batteries. Schematic of a) HT Na-S, b) RT Na-S, c) IT Na-S, and d) the proposed IT K-S battery. By utilizing the liquid K alloy and K^+-conducting β''''-alumina solid electrolyte (K-BASE), we developed a novel IT K-S battery capable of operating at 60 °C. K-BASE suppresses the shuttle effect of soluble polysulfides and prevents dendrite formation. The catholyte comprises diglyme (DEGDME), a deep eutectic solvent (DES, 1:1 acetamide/ε-caprolactam), and dissolved polysulfides, with carbon cloth acting as a conductive substrate and catalyst support. e) Discharge–charge voltage profiles of IT K-S batteries with/wo catalyst and DES.

Despite these advancements, IT Na-S batteries still encounter critical challenges, particularly poor sodium wettability at the Na/BASE interface.[18] This issue arises from the formation of sodium oxide at the Na/BASE interface, which hinders sodium dissolution and Na^+ transport across the interface.[19] Various methods have been explored to address this problem, such as coating the BASE surface with lead or tin,[20] or replacing metallic sodium with Na-Cs alloy.[21] However, these approaches have shown limited effectiveness at temperatures below 100 °C.[22] Lu et al. demonstrated that K-Na alloy exhibits effects similar to those of Na-Cs alloy at room temperature.[23] However, when K-Na alloy comes into contact with Na^+-conducting BASE, it can cause BASE fracture due to the higher thermodynamic stability of K^+ within the BASE structure.[24,25] To capitalize on the advantages of K-Na alloy, the focus has been further directed toward IT K-S batteries in pursuit of more promising solutions.

IT K-S batteries also face similar challenges in cathode design as IT Na-S batteries. The discharge products of K_2S_2 and K_2S are poorly conductive and insoluble, which slows reaction kinetics and increases electrode polarization.[26] To address this issue, we previously proposed a new family of amide electrolytes that shows reasonable K_2S_2/K_2S solubility and increases capacity from ≈400 to 600–800 mAh g^{-1}.[6] Nonetheless, the high viscosity of these electrolytes hinders ion transport.[27] And their reliance on polysulfide solubility to enhance sulfur redox reactions presents challenges for further improving battery capacity and long-term stability.

Herein, we propose a dual-functional interfacial regulation strategy that integrates a deep eutectic solvent (DES) with a NiS catalyst to overcome persistent challenges in IT K-S batteries (Figure 1d). This approach addresses two critical bottlenecks: the poor solubility of low-order discharge products and the sluggish kinetics of their conversion. Specifically, DES enhances the solubility and interfacial reactivity of K_2S_2/K_2S through strong coordination, while also forming moderate electronic interactions with NiS to modulate adsorption strength and suppress catalyst deactivation. This synergistic regulation extends the reduction pathway toward the formation and reversible conversion of K_2S_2/K_2S, ultimately enabling high sulfur utilization and stable long-term cycling (Figure 1e). Consequently, this K-S system achieves an initial capacity of 810 mAh g^{-1} at 4 M [S] (6 mg cm^{-2}), with 78% capacity retention over 1300 cycles. Increasing the loading to 8 M [S] (12 mg cm^{-2}) with lean catholyte of 4.2 µL $mg_{[sulfur]}^{-1}$, the cell maintains a capacity of 521 mAh g^{-1}, retaining 84.3% over 500 cycles. These enhancements yield an energy density exceeding 150 Wh kg^{-1} at the cell level, presenting substantial annual cost savings of up to $158k /MW. Techno-economic analysis shows that the developed IT K-S battery promises a competitive levelized cost of storage (LCOS) of $140 /MWh for long-duration energy storage.

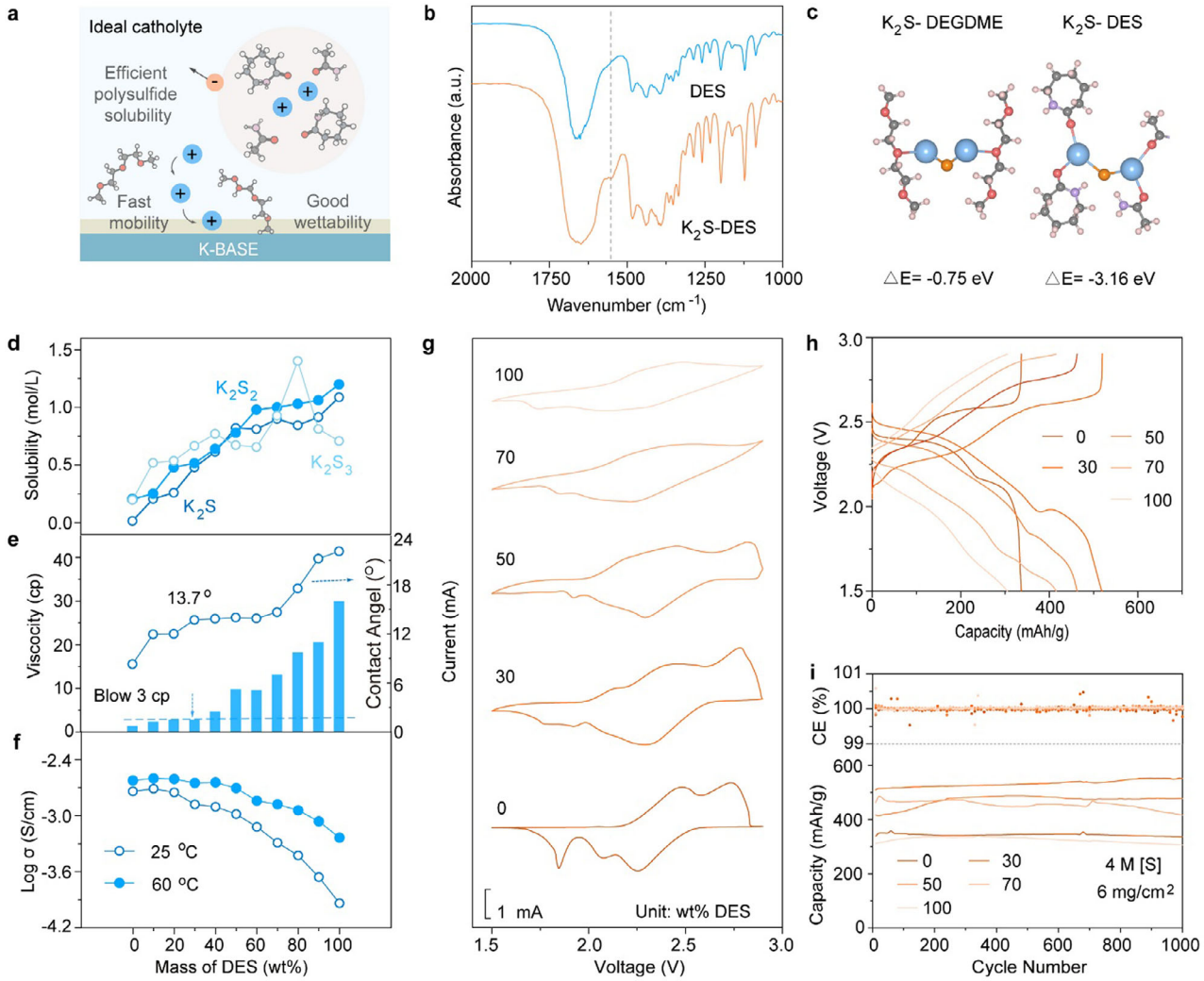

Figure 2. Catholyte Design and Optimization with DES. a) Schematic illustration of an ideal catholyte system. b) FTIR spectra of DES and 0.5 M K_2S dissolved in DES. c) Adsorption configurations and energies of K_2S with DEGDME and DES. d) Solubility of K_2S_3, K_2S_2, and K_2S in catholytes with varied DES content (wt.% DES) at 60 °C. e) Viscosity analysis and contact angle measurements of catholyte with varied DES content on K-BASE. f) Ionic conductivity of catholytes at room temperature and 60 °C. g) CV curves of 4 M [S] cells. h) Initial charge–discharge profiles, and i) cycling performances of 4 M [S] cells with varied DES content- catholyte at 1.5 mA cm^{-2}. All electrochemical measurements were performed at 60 °C (unless otherwise specified) to ensure sufficient ionic conductivity and minimize interfacial resistance, as lower temperatures impaired performance.

2. Results

2.1. Design Principle for DES-Based Catholyte

The design principles of the catholyte for high-performance intermediate-temperature (IT) K-S batteries highlight the critical role of key intermolecular interactions, including solvent-solvent and solvent-polysulfide interactions. Weak interactions between solvent molecules lower electrolyte viscosity and improve ionic conductivity. Conversely, strong interactions with potassium polysulfides enhance polysulfide solubility and capacity, particularly for low-order species (Figure S1, Supporting Information).[28] Achieving an optimal balance between these properties requires a carefully tailored combination of solvents to maximize fluidity, ionic conductivity, and redox kinetics (**Figure 2a**).

Diglyme (DEGDME) was selected as the primary solvent due to its excellent fluidity and stable ionic conductivity. In contrast, 1,3-Dioxolane/Dimethoxymethane (DOL/DME) was excluded because of its high volatility and safety concerns. Tetraglyme (TEGDME) was also found impractical due to its high viscosity. (Note S1, Supporting Information) Despite these advantages, DEGDME exhibits weak interaction with low-order polysulfides and limitis its potential to further improve capacity.

To overcome the limited solubility in DEGDME, DES was introduced as a co-solvent to enhance polysulfide coordination and dissolution. DES promotes K_2S dissolution through strong coordination between K^+ and the C=O groups, and weak hydrogen bonding between sulfur species and –NH– groups. Fourier Transform Infrared (FTIR) revealed a new peak at 1550 cm^{-1} (Figure 2b), indicating C=O···K^+ coordination,[29] while DFT confirmed a significantly stronger binding energy than that in

DEGDME (Figure 2c). Moreover, DES supports a higher coordination number, enabling more efficient dissociation of solid K_2S. Density Functional Theory (DFT) also indicates a weak interaction between sulfur atoms and –NH– groups in K_2S-DES system (Figure S2, Supporting Information), which is supported by a Raman signal at 2572 cm^{-1} (Figure S3a, Supporting Information) and a Proton Nuclear Magnetic Resonance (^1H NMR) shift at 1.86 ppm (Figure S3b, Supporting Information), consistent with H···S hydrogen bonding.[30,31] These results demonstrate that DES enhances K_2S solubility by enabling a favorable solvation environment. However, the high viscosity of DES and its poor wettability toward K-BASE necessitate an optimized formulation to achieve a balance among solubility, fluidity, and interfacial compatibility.

30 wt.% DES was identified as the optimal composition, which effectively addresses the challenges of solubility, viscosity, and wettability with K-BASE. This composition utilizes the strong interaction between DES and lower-order polysulfides to achieve reasonable dissolution capacities for K_2S_x (x = 1–3) at 60 °C. The measured values are 0.48, 0.52, and 0.67 M, respectively (Figure 2d). Such solubility expands sulfur utilization in the battery and thereby enhances its capacity. Additionally, the viscosity of 30 wt.% DES (Figure 2e, 2.86 cp) was significantly reduced compared to 100 wt.% DES (29.96 cp), aligning closely with commercial electrolyte standards (3 cp). The excellent wetting properties of this formulation were evidenced by a contact angle of 13.7° with K-BASE (Figure 2e), which enables efficient ion transport and reduces interfacial resistance.

To further assess the electrochemical properties of the catholyte in K-S batteries, electrochemical impedance spectra (EIS) measurements were employed to investigate ionic conductivity and charge transfer resistance. Measurements revealed that 30 wt.% DES achieved ionic conductivities of 1.35×10^{-3} S/cm at room temperature and 2.24×10^{-3} S cm^{-1} at 60 °C, indicating excellent ion transport (Figure 2f). K-S cells tested with 4 M [S] and varied DES contents displayed low charge transfer resistance for both 0 and 30 wt.% DES (Figures S4, S5, and Note S2, Supporting Information). However, 0 wt.% DES exhibited a diffusion tail at 280 mAh g^{-1} with a diffusion coefficient of 1.29×10^{-14} cm^2 s^{-1}, indicating limited ion transport caused by the insolubility of polysulfides and sulfides (Note S3, Supporting Information). In contrast, other electrolytes showed negligible diffusion tails.

Cyclic voltammetry (CV) was conducted to further explore the role of DES in enhancing polysulfide conversion and overall electrochemical performance. CV results showed that the 30 wt.% DES exhibited the largest peak area, which indicates a higher degree of polysulfide involvement in the electrochemical reactions (Figure 2g; Note S4, Supporting Information). This is a key factor in achieving the highest initial capacity of 520 mAh g^{-1} (Figure 2h) in the K-S cells using 30 wt.% DES. Furthermore, the minimal capacity loss over 1000 cycles and a near-100% Coulombic efficiency (Figure 2i) suggest that the 30 wt.% DES electrolyte system not only enhances the polysulfide conversion but also maintains long-term stability with negligible side reactions.

Despite the effective polysulfide conversion achieved with 30 wt.% DES (30DES), its capacity remains restricted to the reduction of K_2S_3, accounting for only one-third of the theoretical value. Achieving higher capacity requires extending the final reduction products to K_2S_2 and K_2S. This process relies on catalysts designed to facilitate deep reduction reactions and maximize the energy storage potential.

2.2. Redox Products Optimization in the 30DES System

To overcome the reduction limit of K_2S_3 in the 30DES system and enable the formation of K_2S_2 and K_2S, catalysts must be tailored to promote deep polysulfide conversion. The choice of an optimal catalyst depends on the specific structural and chemical characteristics of the battery system. In Li-S batteries, catalysts mainly serve to suppress shuttle effects and facilitate the solid–liquid–solid conversion to Li_2S.[32] In contrast, IT K-S batteries employ a closed catholyte structure with BASE, which effectively blocks polysulfide migration. Under this configuration, the role of the catalyst shifts toward regulating interfacial adsorption and enabling the reversible conversion of K_2S_2 and K_2S in a polar liquid-phase environment. Phosphides that are effective in Li-S systems may therefore offer limited benefits here.[33,34] Nickel sulfide (NiS), by comparison, exhibits better compatibility with both DES and K_2S, motivating its further investigation alongside other nickel-based materials such as Ni_2P and NiO.

Based on this mechanistic distinction, we next evaluate the selection criteria and structural characteristics of candidate nickel-based catalysts. An ideal catalyst for this system should meet two criteria: 1) a balanced adsorption strength in the 30DES system that facilitates the rapid conversion of polysulfides to lower-order sulfides (K_2S_2/K_2S), and 2) low-cost, abundant materials suitable for large-scale production. Nickel-based catalysts were chosen due to their moderate binding energy with polysulfides, which enables efficient catalytic conversion.[35,36] Additionally, Ni is earth-abundant, cost-effective, and widely used in sulfur-based electrochemical systems.[37] Among the selected nickel-based catalyst NiX (X = S, O, P), their crystal structures and morphology were characterized. X-ray diffraction (XRD) analysis confirmed the crystal structures of NiS, NiO, and Ni_2P (**Figure 3a**), while scanning electron microscopy (SEM) revealed that these catalysts form sheet-like structures on carbon cloth (Figure S6, Supporting Information). NiS was identified as the optimal choice, and its advantages will be discussed in detail below. Transmission electron microscopy (TEM) demonstrated the crystalline of NiS with a lattice spacing of 2.59 Å. Elemental mapping showed a uniform distribution of sulfur and nickel, indicating a homogeneous composition that facilitates efficient catalytic conversion (Figure 3b).

To understand the polysulfide reduction of the three nickel-based catalysts, CV measurements were conducted. Among NiO, Ni_2P, and NiS, the latter exhibited the largest peak area and the highest current response during the reduction process. Notably, it featured a prominent reduction peak at 1.60 V (Figure 3d), corresponding to the final step of K_2S_2 to K_2S conversion. Additional reduction peaks at ≈2.35 V, 1.96 V, and 1.80 V are assigned to the stepwise reductions of K_2S_6 to K_2S_4, K_2S_4 to K_2S_3, and K_2S_3 to K_2S_2, respectively.[38] During the anodic scan, the oxidation peaks at 2.10, 2.45, and 2.75 V correspond to the oxidation of K_2S/ K_2S_2, intermediate species such as K_2S_3–K_2S_4, and the regeneration of higher-order polysulfides such as K_2S_6.[39] These peak assignments are consistent with the S/K ratios determined in the catholyte after interrupted cycling (Figure S7, Supporting Information). This enhanced conversion of low-order

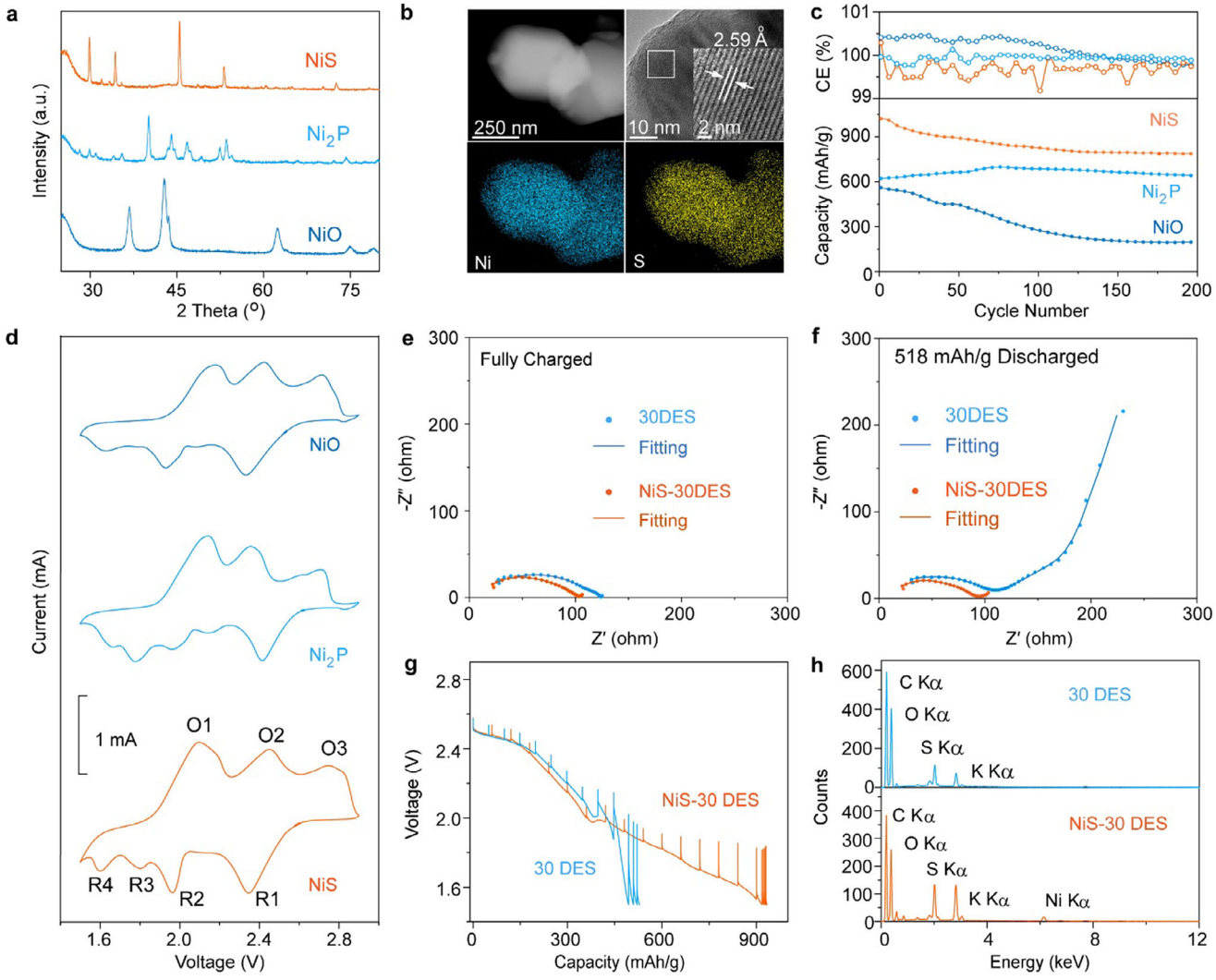

Figure 3. Catalytic Activity and Reduction Product Characterizations. a) XRD patterns of nickel-based catalysts. b) HRTEM image, HAADF-STEM image, and corresponding EDS mapping of NiS. c) CV curves and d) cycling performances of K-S batteries with 4 M [S] and NiX-30DES catholyte (X = O, S, P). EIS results of NiS-DES and DES-based cells with 4 M [S] e) in the fully charged state, and f) at a discharged capacity of 518 mAh g^{-1} (1 to 10 MHz). g) GITT measurements for the discharge process of 30DES and NiS-30DES cells with 4 M [S]. Each 30-min discharge is immediately followed by a 10-min rest period. h) EDS results of the carbon cloth in NiS-30DES and 30DES cells after the 10th cycle using 4 M [S].

species in NiS-30DES batteries leads to a high discharge capacity of 1066 mAh g^{-1}, corresponding to 65% sulfur utilization, which significantly exceeds the values achieved with Ni_2P (37.5%) and NiO (35.1%) (Figure S8, Supporting Information). In addition, cycling performance tests were conducted to assess the stability of each catalyst. After 200 cycles at 1.0 mA cm^{-2}, the NiS-30DES cell retained 95% of its capacity, while NiO retained only 34% (Figure 3c). These findings provide further evidence of the effectiveness of NiS in improving both capacity and stability for battery applications.

We further performed EIS to understand how NiS affects electrochemical performance. The 30DES and NiS-30DES cells exhibit low impedance at full charge, indicating fast kinetics in the redox reactions of high-order polysulfides (Figure 3e). The negligible diffusion tail suggests rapid ion transport in the liquid phase. However, when discharged to 518 mAh g^{-1} (99.6% of the discharge capacity in 30DES), the 30DES electrolyte showed a pronounced diffusion tail with a coefficient of 4.57×10^{-16} cm^2 s^{-1}. This result confirms slow kinetics and poor ion transport of solid low-order polysulfides (Note S3, Supporting Information). In contrast, the NiS-30DES cell showed no significant diffusion tailing (Figure 3f) and the liquid-phase diffusion coefficient of 1.17×10^{-8} cm^2 s^{-1} further confirmed the enhanced polysulfide conversion facilitated by NiS. These observations were further validated through equivalent circuit fitting of the EIS spectra (Note S5 and Figure S9, Supporting Information). The discharged 30DES cell required two Warburg components (10.24 and 172.7 Ω), indicating severe diffusion limitations due to solid K_2S_2/ K_2S accumulation. In contrast, the NiS–30DES cell was well fitted using a single Warburg element (22.98 Ω), highlighting improved ion transport and mitigated diffusion polarization at deep discharge.

To evaluate the sluggish kinetics of K_2S_2/K_2S conversion under realistic conditions, Galvanostatic Intermittent Titration Technique (GITT) was conducted at 1.5 mA cm^{-2}, consistent with the cycling current (Figure 3g). At 518 mAh g^{-1}, the 30DES cell exhibited a high overpotential of ≈0.5 V, while the NiS–30DES cell showed only ≈75 mV, confirming the catalytic effect of NiS in lowering the energy barrier for low-order polysulfide conversion. The 10-min rest period allowed clear voltage relaxation in both systems. Additional GITT tests at 0.5 mA cm^{-2} with 60-min rests produced consistent overpotential trends, validating the reliability of the original protocol (Figure S10, Supporting Information). These findings underscore the role of NiS in promoting polysulfide conversion and improving electrochemical performance.

To further confirm the efficient conversion of polysulfides, XRD and energy-dispersive spectroscopy (EDS) were employed to analyze the discharge products. XRD analysis identified K_2S_3 as the primary discharge product in the 30DES system, while K_2S and K_2S_2 were dominant in NiS-30DES cells (Figure S11, Supporting Information). Subsequently, EDS was employed for quantitative analysis of the sulfur-to-potassium (S/K) ratios. The results identified a S/K ratio of 0.75 in the NiS-30DES system at 4 M [S] (Figure 3h; Figure S12a, Supporting Information) and 0.46 at 1 M [S] (Figure S13, Supporting Information), confirming the enhanced sulfur conversion to K_2S. In contrast, the 30DES system showed a higher S/K ratio of 1.5, indicating incomplete sulfur conversion (Figure 3h; Figures S12b and S14, Supporting Information). These findings indicate that DES alone fails to reduce polysulfides beyond K_2S_3, while the NiS–DES system enables further conversion to K_2S_2 and K_2S, facilitating enhanced discharge capacity and prolonged cycling.

To further verify the composition of species remaining in the catholyte near the end of discharge, we conducted EDS mapping on the catholyte of the NiS–30DES system at 1.5 V. The S/K ratio was found to be 0.72, which closely matches the value observed on the carbon cloth surface (Figure S15, Supporting Information). This suggests that K_2S_2/K_2S remain partially dissolved in the liquid phase, forming a dynamic precipitation–dissolution equilibrium with the solid phase. It is important to note that a S/K ratio below 1 does not definitively exclude the coexistence of K_2S and K_2S_3. To address this, we conducted an auxiliary experiment by introducing K_2S into prepared K_2S_3 or K_2S_2 solutions (Figure S16, Supporting Information). The addition of K_2S significantly lightened the color of the K_2S_3 solution, resembling that of K_2S_2, while K_2S_2 solution showed no notable change. This indicates that in the presence of K_2S, K_2S_3 tends to convert to K_2S_2, and a stable coexistence of K_2S and K_2S_3 is thermodynamically unfavorable.

2.3. Mechanism of Synergistic Effect

To further elucidate the mechanisms underlying the enhanced sulfur conversion and utilization in the NiS–DES system, density functional theory (DFT) calculations were performed. In our modeling, K_2S was selected as the adsorption species, as it is the dominant discharge product and its reversibility plays a crucial role in capacity retention. Although both NiS and K_2S are solid-phase materials, experimental results have demonstrated that K_2S exists not only as a crystalline precipitate but also partially dissolves in the highly polar DES environment, thereby participating in interfacial reactions. Moreover, due to the known scaling relationship among sulfur intermediates, the adsorption behavior of K_2S can qualitatively reflect that of other low-order species.[40–42] The results revealed that DES maintains a balanced interaction between K_2S intermediates and the catalyst, reducing excessive interactions with polysulfides. This effect minimizes catalyst deactivation and enhances K_2S activation through strong electron transfer between K_2S and the solvent (**Figure 4a**). More details are provided about the mechanistic rationale for NiS–DES synergy in Note S6 (Supporting Information). Building on this understanding, we further compared the interfacial environments in solvent-free, DEGDME, and DES systems (Note S7, Supporting Information). The results confirmed that DES offers a uniquely favorable coordination environment, essential for regulating sulfur redox kinetics and enabling efficient conversion of terminal species.

In the catalyst-K_2S system without solvents, the catalysts showed high adsorption energies with K_2S (Figure 4b, NiS: −5.07 eV, Ni_2P: −6.26 eV, NiO: −5.54 eV), indicating strong catalyst-polysulfide interactions (Figure 4c; Figure S17a,b, Supporting Information). Differential charge density analysis (DCDA) revealed the strong interactions between catalysts and K_2S, with significant charge transfer observed (Figure 4f; Figure S17c,d, Supporting Information). Though the strong interaction promoted initial adsorption and conversion, they also caused severe catalyst poisoning, which hindered subsequent charge–discharge processes.

To mitigate catalyst poisoning and enhance K_2S conversion, solvent molecules were introduced into the models to regulate interactions between catalysts and K_2S. For the catalytic system containing catalysts and solvents, there are two parts of interactions: catalysts-solvents and solvents-K_2S. The synergetic effect of catalysts and solvent influence the adsorption and conversion of K_2S. For the catalyst-K_2S-DEGDME system, the adsorption energies were relatively weak (Figure 4b,d; Figure S18a,b, Supporting Information, NiS: −2.94 eV > Ni_2P: −2.33 eV > NiO: −2.19 eV). Further insights into the mechanism were provided by DCDA, which demonstrated minimal electron transfer between the catalyst and DEGDME, as well as between DEGDME and K_2S (Figure 4g; Figure S18c,d, Supporting Information). Therefore, the weak interactions between the catalysts and DEGDME alleviated catalyst poisoning in the catalyst-K_2S system. However, the weak interaction between the solvent and K_2S suppressed K_2S activation, limiting the reversible conversion of low-order polysulfides during charge-discharge cycles. These findings well explain the experimental phenomena. The differential capacity (dQ/dV) curves showed no distinct reaction plateaus below 2.0 V, and the initial sulfur capacity of the NiX-0 DES system exhibited only a slight improvement over the 0DES battery (Figure S19, Supporting Information). This limitation can be attributed to the insufficient activation of K_2S in the catalyst-K_2S-DEGDME system. Moreover, UV–vis spectroscopy showed that adsorption capacities followed the order NiS > Ni_2P > NiO (Figure S20, Supporting Information) in the DEGDME environment.

Building on the stronger interaction between DES and K_2S, subsequent studies explored how DES regulates catalytic performance in the catalyst-K_2S-DES system. The adsorption

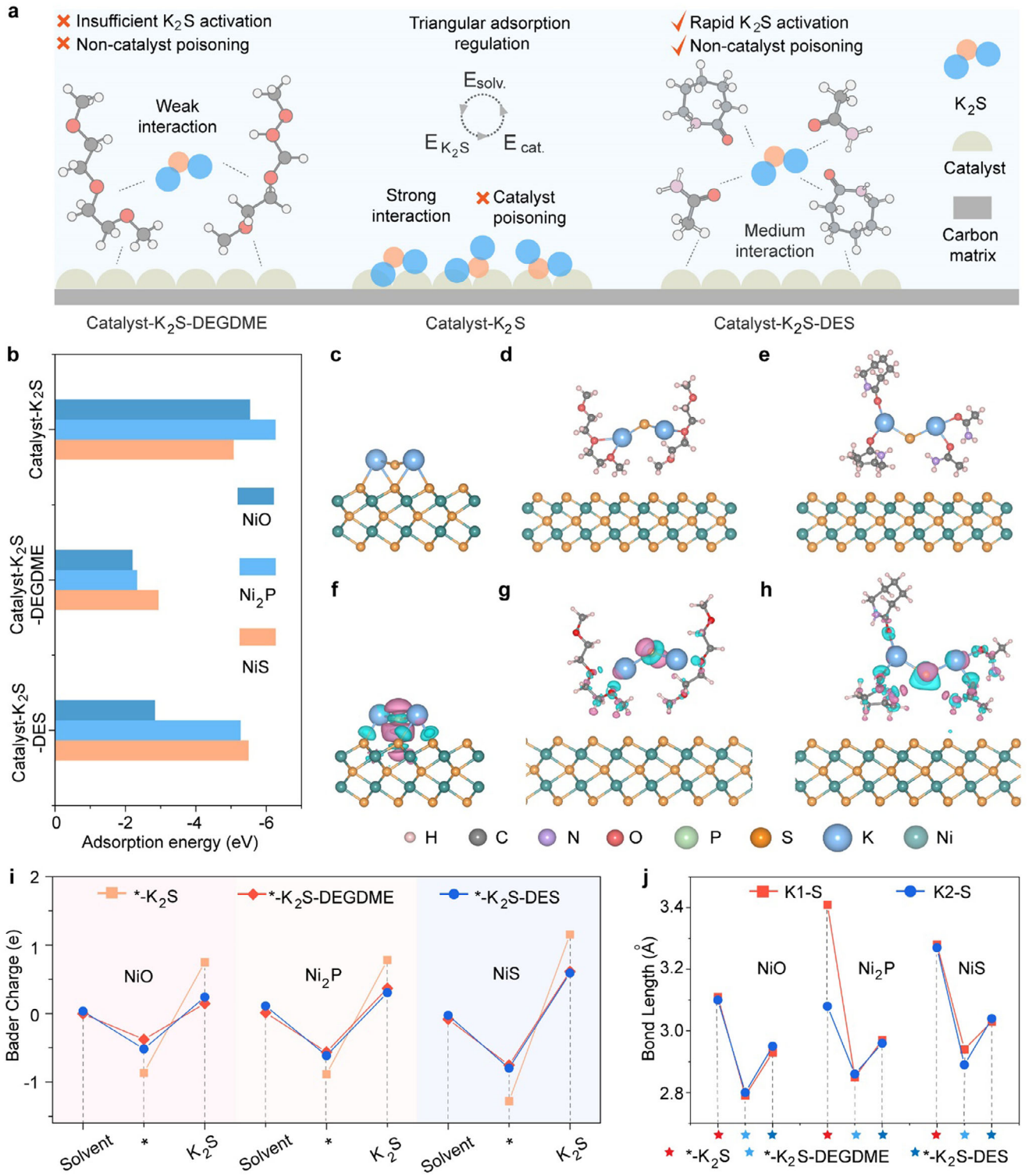

Figure 4. DFT calculation and result analysis. a) Schematic of the influence of solvents on the catalytic process. b) Adsorption energies of K_2S with all systems. Optimized structures of c) NiS-K_2S, d) NiS-K_2S-DEGDME, and e) NiS-K_2S-DES. Differential charge densities of f) NiS-K_2S, g) NiS-K_2S-DEGDME, and h) NiS-K_2S-DES. The isosurface level was 0.003 e·bohr^{-3}. i) Bader charge analysis of catalys-K_2S, catalyst-K_2S-DEGDME, and catalyst-K_2S-DES systems. j) Bond length of K-S bonds in all systems. K_2S shows two K–S bonds, which is K1-S and K2-S. Here, * is referred to the catalyst.

energies followed the order NiS (−5.50 eV) >Ni_2P (−5.27 eV) >NiO (−2.84 eV) (Figure 4b), indicating that DES significantly enhanced the interactions among K_2S, solvent, and catalysts compared to the DEGDME system. While NiO exhibited insufficient adsorption strength to effectively activate K_2S (Figure S21a, Supporting Information), the adsorption energies for NiS-K_2S-DES and Ni_2P-K_2S-DES systems increased substantially (Figure 4e; Figure S21b, Supporting Information). The enhancement in adsorption energy can be attributed to the interaction between the catalysts and solvent molecules and that between solvent molecules and K_2S. DCDA revealed weak electron transfer between DES and catalysts, which effectively alleviated catalyst poisoning. Meanwhile, strong electron transfer between DES and K_2S facilitated K_2S activation, enabling its reversible participation in redox reactions (Figure 4h; Figure S21c,d, Supporting Information). These insights underscore the dual roles of DES in stabilizing catalysts while promoting K_2S activation, establishing it as a superior solvent for catalytic systems. The computational predictions were validated experimentally. dQ/dV curves displayed distinct reaction plateaus at 1.6 and 1.9 V, with NiS showing the highest plateaus, followed by Ni_2P and NiO (Figure S22, Supporting Information). Sulfur capacity tests in the 30DES system further supported these findings, with capacities measured as NiS (1066 mAh g^{-1}) >Ni_2P (600 mAh g^{-1}) >NiO (580 mAh g^{-1}) >no catalyst (510 mAh g^{-1}).

To offer more quantitative evidence of the underlying mechanisms of solvents roles, we analysis the Bader charge transfer and bond length changes for the NiO/Ni_2P/NiS catalysts with and without solvents. In the solvent-free system, substantial electron transfer occurred between the catalysts and K_2S (Figure 4i). Meanwhile, the K–S bond length increased significantly (Figure 4j), further confirming the strong activation of K_2S and the severe poisoning of the catalyst. When DEGDME was introduced, the electron transfer between the catalysts and K_2S decreased notably (Figure 4i). And the K–S bond length shortened (Figure 4j), reflecting insufficient activation of K_2S. Therefore, although weaker interactions with DEGDME reduced catalyst poisoning, they failed to enable efficient activation and restricted the reversible conversion of low-order polysulfides during charge–discharge cycles.

Compared to solvent-free and DEGDME systems, DES significantly enhanced the stability of catalysts and improved the interactions with K_2S. Electron transfer between DES and K_2S increased significantly relative to DEGDME, while electron transfer between the catalysts and K_2S decreased compared to the solvent-free system (Figure 4i). This moderate electron transfer achieved a balance by mitigating catalyst poisoning and enhancing the activation of K_2S. Meanwhile, the K–S bond length increased relative to the DEGDME system (Figure 4j). This further highlights the ability of DES to promote K_2S activation and act as an effective solvent for catalytic systems.

2.4. Catalytic Performance and Electrochemical Stability

To further evaluate the effect of the NiS-30DES system on sulfur conversion and electrochemical performance in IT K-S batteries, we first conducted battery tests using a 1 M [S] catholyte. The NiS-30DES cell achieved an initial capacity of 1659 mAh g^{-1}, which is close to the theoretical value of 1675 mAh g^{-1} (**Figure 5a**). After 1000 cycles, the capacity remained at 738 mAh g^{-1}, demonstrating efficient sulfur reduction to K_2S and enhanced discharge capacity (Figure 5b). In contrast, the capacity of the 30DES cell stabilized at 545 mAh g^{-1} over 1000 cycles, showing that K_2S_3 was the final reduction product. Notably, the NiS–30DES cell under 1 M [S] conditions exhibited unique capacity evolution behavior. Initially, the high reaction kinetics driven by low polysulfide concentration enabled a high discharge capacity. However, rapid formation and local accumulation of low-order species (K_2S_2 and K_2S) at high current density (1 C, corresponding to 1.5 mA cm^{-2}) led to partial electrode passivation and subsequent capacity decline. With continued cycling, improved catholyte wetting and gradual dissolution of deposited species facilitated the establishment of a more effective catalytic interface. This interfacial evolution enhanced reaction reversibility, causing the observed capacity recovery around the 550th cycle and eventual capacity stabilization.

To further enhance the sulfur loading and energy density of K-S batteries, we tested 4 and 8 M [S] electrolytes and evaluated the stability and discharge capacity of these systems over extended cycles. These batteries exhibit remarkable efficiency and stability. At a 100% state of saturation (SOS), the 4 M[S] and 8 M[S] batteries sustained reversible cycling for 1300 and 500 cycles, respectively. This demonstrates the strong cycling stability achieved through this dual-functional strategy. These systems support extended cycle life and minimize active material loss with Coulombic efficiency exceeding 99.95% (Figure 5c,d).

The NiS-30DES cell with 4 M [S] (sulfur loading of 6 mg cm^{-2}) exhibited an initial discharge capacity of 810 mAh g^{-1} at 1.5 mA cm^{-2}, which gradually increased to 865 mAh g^{-1} by the 180-th cycle and remained stable at 601 mAh g^{-1} after 1300 cycles (0.02% capacity decay/cycle, Figure 5c). The capacity increase may be attributed to the gradually enhanced interaction between NiS and the active material during cycling. This effect is more significant in high-sulfur-concentration catholyte due to their higher viscosity. In comparison, the 30DES cell maintained a stable capacity of ≈520 mAh g^{-1} but exhibited a sudden failure at the 1254-th cycle. The absence of NiS likely led to polysulfide accumulation and sluggish redox kinetics, causing electrode passivation and eventual failure.

Increasing the sulfur concentration in the catholyte from 4 to 8 M lowered the catholyte-to-sulfur (C/S) mass ratio from 8.4 to 4.2 μL $mg_{[sulfur]}^{-1}$. This reduction is a key characteristic of lean catholyte systems operating under more stringent conditions. Remarkably, the NiS-30DES cell maintained excellent performance. It delivered an initial capacity of 521 mAh g^{-1}, which increased to 585 mAh g^{-1} by the 60-th cycle, with a capacity of 493 mAh g^{-1} after 500 cycles (12 mg cm^{-2} sulfur, 0.03% capacity decay/cycle, Figure 5d). In contrast, the 30DES cell maintained only 410 mAh g^{-1}. These results further demonstrate the effectiveness of integrating DES with a tailored catalytic interface to enhance the cycling performance of IT K-S batteries.

To further assess the stability of this system under diluted catholyte conditions, we tested the NiS–30DES cell with a higher catholyte-to-sulfur (C/S) ratio of 5.1 μL mg^{-1} at a sulfur concentration of 6.5 M [S] and a loading of 12 mg cm^{-2}. The cell delivered an initial capacity of 537 mAh g^{-1} (Figure S23, Supporting Information), which is slightly higher than the value obtained

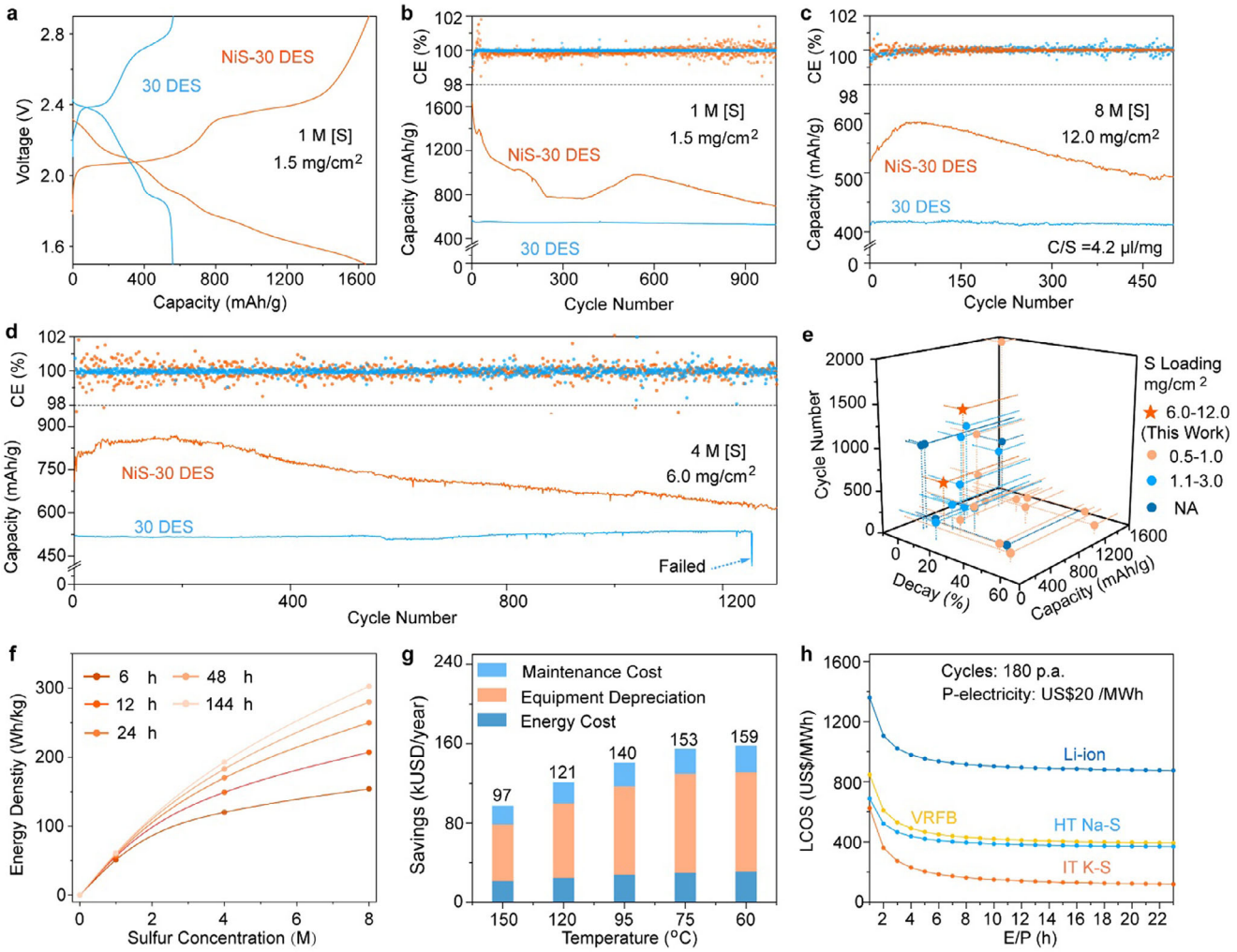

Figure 5. Electrochemical Performances and Techno-economic Analysis in DES-Based IT K-S Batteries. a) Charge–discharge voltage profiles and b) cycling performances of NiS-30DES and 30DES K-S batteries with 1 M [S] at 1.5 mA cm^{-2}. Cycling performances of K-S batteries with c) 4 M [S] and d) 8 M [S] catholyte at 1.5 mA cm^{-2}. e) Comparison of specific capacity and cycling performance of NiS-30DES with the state-of-the-art solutions for K-S batteries reported. A more detailed comparison with state-of-the-art K-S battery systems is provided in Note S8 (Supporting Information). f) Relationship between actual energy density and sulfur concentration in IT K-S batteries at different discharge durations. g) System cost savings achieved by lowering the operating temperature compared to operation at 350 °C. h) LCOS analysis of lithium-ion battery (Li-ion), high-temperature sodium-sulfur battery (HT Na-S), vanadium redox flow battery (VRFB), and IT K-S as a function of discharge duration E/P (180 cycles per annum (p.a.), interest rate 8%, electricity price (P-electricity) US$ 20/MWh).

at 8 M [S], indicating its stable electrochemical behavior. Additionally, the thermal and electrochemical stability of the 30DES catholyte were confirmed through thermogravimetric analysis (TGA) and linear sweep voltammetry (LSV). TGA measurements revealed a gradual mass loss of ≈4.9 wt.% at 60 °C (Figure S24a, Supporting Information), attributed to slow solvent evaporation rather than decomposition. LSV curves exhibited no significant increase in current between 1.5 and 2.9 V (Figure S24b, Supporting Information), validating its electrochemical inertness. To further evaluate the physicochemical stability of 30DES, we monitored its viscosity and ionic conductivity over 9 days at 60 °C. The viscosity increased slightly from 1.98 to 2.47 cP, while the conductivity remained stable at ≈2.4 × 10^{-3} S cm^{-1} (Figure S24c, Supporting Information). These results confirm the long-term stability of 30DES under thermal operation.

To clarify the mechanistic innovation and advantages of the NiS–DES system, we compared the NiS–30DES system with representative K-S battery strategies, including room-temperature designs (e.g., SPAN,[43–46] small-molecule sulfur[47–50]) and intermediate-temperature catholytes (e.g., TEGDME,[23,51] eutectic solvents[6]) in both Figure 5e and Note S8 (Supporting Information). Most prior systems are limited by either low sulfur loading, short cycle life, or insufficient discharge capacity under practical conditions. While SPAN offers structural stability, its low sulfur content (<40 wt.%) restricts capacity. Small-molecule sulfur exhibits high reactivity but suffers from instability at high loading. Conventional TEGDME-based catholytes display poor solubility for short-chain polysulfides, whereas eutectic solvents face challenges in viscosity and diffusion.

Despite extensive efforts in catalyst design,[52–57] electrolyte tuning,[58,59] carbon host engineering[60–64] and interface wettability,[21,65] it remains difficult to simultaneously achieve high capacity, long cycle life, and low polarization under high sulfur loading due to incomplete polysulfide conversion and interfacial passivation. In contrast, the NiS–30DES system demonstrates a favorable balance between reactivity and stability, enabling reversible cycling over 500–1300 cycles at sulfur loadings of 6–12 mg cm^{-2}.

To further clarify the respective roles of DES and NiS in performance enhancement, we conducted a comparative analysis of four systems: 0DES, 30DES, NiS–30DES, and NiS–0DES (Figure 1e). When DEGDME is used alone (0DES), the limited solubility for short-chain polysulfides yields a capacity of only ≈350 mAh g^{-1}. Adding 30 wt.% DES (30DES) improves solubility and coordination with K_2S_x, increasing the capacity to 585 mAh g^{-1}. However, the system still fails to fully convert K_2S_2/K_2S. Upon introducing NiS (NiS–30DES), the capacity reaches 1067 mAh g^{-1}, indicating enhanced catalytic conversion. In contrast, the NiS–0DES system delivers only ≈195 mAh g^{-1}, suggesting that NiS alone is insufficient without solvent mediation. These comparisons reveal that DES not only facilitates polysulfide dissolution and activation but also modulates catalyst–sulfur interactions, preventing surface deactivation and enabling efficient interfacial conversion.

To further evaluate the long-term stability of NiS, we analyzed its surface chemistry and morphology at the pristine state, after 50 cycles, and after 2000 cycles. XPS results showed that NiS remained stable initially but developed surface passivation over extended cycling due to accumulated polysulfides and oxidative byproducts (Figure S25a,c,e, Supporting Information). The S 2p spectra indicated significant surface deposition (Figure S25b,d,f, Supporting Information), while SEM images revealed partial detachment and redistribution of NiS sheets on the carbon cloth (Figure S26, Supporting Information). These changes were primarily caused by electrolyte evaporation and interfacial compaction rather than structural decomposition. Corresponding increases in electrochemical polarization and capacity decay were observed in the voltage–capacity profiles (Figure S27, Supporting Information). Despite surface alterations, the bulk NiS structure remained chemically intact. These findings suggest that performance degradation mainly arises from surface coverage, interfacial passivation, and mechanical detachment. This mechanistic understanding underscores the need to improve interfacial stability and reduce solvent volatility in future designs to maintain long-term cycling durability.

2.5. Energy Density and Economic Viability

The IT K-S battery with competitive energy density and material costs demonstrates significant potential for long-duration energy storage. At a discharge time of 12 h, 4 M [S] and 8 M [S] batteries achieve energy density of 150 and 207 Wh kg^{-1} (Figure 5f) and material costs of $35 /kWh and $33 /kWh (Figure S28, Supporting Information), respectively.[66] Increasing discharge duration and sulfur concentration further enhance energy density while driving down material costs. For an 8 M [S] battery with a one-week discharge duration, the energy density exceeds 250 Wh kg^{-1} and material costs decrease to $20 /kWh. Details calculations of energy density and cost can be found in Note S9 (Supporting Information). Furthermore, compared to conventional high-temperature (350 °C) and intermediate-temperature (150 °C) systems, our system operating at 60 °C reduces annual energy costs by $158 and $62 k/MW, respectively. (Figure 5g; Note S10, Supporting Information).

A complementary evaluation of the levelized cost of storage (LCOS) further highlights the economic feasibility of the IT K-S battery.[67] The LCOS calculation was based on experimental cell-level data and material costs from real market values. Operational assumptions followed the Schmidt et al. framework[67] and were implemented via the Energy Storage Ninja platform. We compared LCOS across lithium-ion batteries (Li-ion), high-temperature sodium-sulfur batteries (HT Na-S), vanadium redox flow batteries (VRFB), and the IT K-S battery (Figure 5 and Note S11, Supporting Information). All systems showed a rapid decline in LCOS within the first 1–2 h of discharge and stabilized beyond 10 h. The IT K-S battery with NiS-30DES strategy achieved the lowest LCOS of $140 /MWh with a 12-h discharge, which is significantly lower than that of HT Na-S ($380 /MWh) and VRFB ($410 /MWh). These results highlight the unique capability of the IT K-S battery to maintain economic viability and operational stability over extended durations. This achievement sets a new benchmark for long-duration energy storage systems.

3. Conclusion

This study presents a dual-functional interfacial regulation strategy that combines DES with NiS catalyst to address the irreversible deposition of K_2S_2/K_2S in IT K-S batteries. The DES forms moderate electronic interactions with NiS to weaken the overly strong adsorption of K_2S and mitigate catalyst deactivation. Concurrently, its strong interaction with K_2S facilitates interfacial activation and extends the reduction pathway, thereby promoting highly reversible low-order sulfide conversion and deeper discharge.

The IT K-S battery exhibits excellent performance, retaining 810 mAh g for 1300 cycles at 6 mg cm^{-2} S loading with a decay of 0.02% per cycle. At a higher S loading of 12 mg cm^{-2} and a catholyte-to-sulfur ratio of 4.2 µL $mg_{[sulfur]}^{-1}$, it delivers 521 mAh g^{-1} over 500 cycles with a decay of 0.03% per cycle. With an energy density exceeding 150 Wh kg^{-1} and material costs as low as $ 35/kWh, the system also achieves annual operational savings of ≈$158k/MW when operated at 60 °C. Techno-economic analysis further highlights a competitive levelized cost of storage (LCOS) of $ 140/MWh, outperforming many existing long-duration energy storage technologies. These results underscore the strong promise of the NiS–DES synergistic strategy in enabling cost-effective, scalable, and sustainable energy storage solutions.

4. Experimental Section

Preparation of Deep Eutectic Solvent (DES) and K-Na Alloy: All chemicals were of analytical grade. The deep eutectic solvent was prepared by mixing ϵ-caprolactam (CPL, 99%, Sigma–Aldrich) and acetamide (99%, Sigma–Aldrich) in a 1:1 molar ratio. For the K-Na alloy anode, 400 mg of potassium (98%, Sigma–Aldrich), 100 mg of sodium (99%,

Sigma–Aldrich), and 40 mg of conductive carbon black were uniformly mixed in an aluminum container within an argon-filled glove box.

Preparation of Catholyte: The DES and DEGDME (99%, Sigma–Aldrich) were mixed in various weight ratios (X wt.%, X = 0, 10, 20, 30, 40, 50, 60, 70, 80, 90, 100). Then, 0.5 M potassium bis(trifluoromethanesulfonyl)imide (KTFSI, 99%, Dodochem) was added to create a series of catholyte solutions, labeled as X wt.% DES. Additionally, 0.125, 0.5, or 1 M anhydrous Na_2S (99%, Dodochem) and 0.875, 0.35, or 7 M sulfur were mixed with 30 wt.% DES, and the mixture was stirred at 60 °C to form catholyte solutions with varying sulfur concentrations [S].

Preparation of Catalysts—Preparation of Nickel Precursor: A solution of 600 mg urea, 750 mg nickel nitrate hexahydrate, and 20 mL deionized water was transferred into an autoclave along with a 1.5 × 3 cm piece of carbon cloth. The autoclave was placed in an oven at 120 °C for 6 h, producing nickel precursor-coated carbon cloth.

Preparation of Catalysts—Preparation of Nickel Sulfide (NiS): A solution of 180 mg thioacetamide and 20 mL deionized water was prepared and transferred into an autoclave along with the nickel precursor-coated carbon cloth. The autoclave was heated at 180 °C for 12 h. After washing, nickel sulfide-coated carbon cloth was obtained.

Preparation of Catalysts—Preparation of Nickel Oxide (NiO): The nickel precursor-coated carbon cloth was heated in a muffle furnace at 300 °C for 3 h, resulting in nickel oxide-coated carbon cloth.

Preparation of Catalysts—Preparation of Nickel Phosphide (Ni_2P): To prepare nickel phosphide, 500 mg sodium hypophosphite was evenly distributed on the nickel precursor-coated carbon cloth. The sample was heated in an argon-filled tube furnace at 300 °C for 3 h, yielding nickel phosphide-coated carbon cloth.

Characterization: Excess K_2S or K_2S_2 / K_2S_3 (prepared by mixing K_2S and sulfur in 1:1 or 1:2 molar ratios) was added to 11 electrolytes with varying DES concentrations. The mixtures were stirred at 60 °C for 12 h, then settled at 60 °C for another 12 h. The supernatant was diluted, and K^+ concentration was tested by Inductively Coupled Plasma Optical Emission Spectroscpy (ICP-OES) Measurement (Thermo Fisher iCAP6000). Viscosity was measured at 60 °C using a Brookfield LV DV3T viscometer for 11 electrolytes with varying DES content. Contact Angle between the electrolyte solutions and K-BASE was measured using a DataPhysics OCA 15Pro contact angle meter. X-ray Diffraction (XRD) Analysis was performed on a Bruker D8 Advance over 20–80° for 4 M [S] batteries after 10 cycles. Carbon cloth cathodes were extracted and analyzed in sealed holders. Fourier transform infrared (FTIR) spectra were collected using a PerkinElmer Frontier spectrometer over 400–4000 cm^{-1} with a resolution of 4 cm^{-1}.Transmission electron microscopy (TEM) images and corresponding EDS mapping were recorded by JEOL JEM-F200. Raman spectra were acquired using a 532-nm diode laser on Horiba LabRAM HR Evolution with a range from 500 to 3500 cm^{-1}.^{1}H Nuclear Magnetic Resonance (NMR) measurement was conducted on BRUKER AVANCE III HD 600. All samples were dissolved by dimethyl sulfoxide-d6 first and the identification of the peaks is realized by MestReNova. Imaging and (EDS) Element Mapping. Scanning Electron Microscopy (SEM) imaging and Energy Dispersive Spectroscopy (EDS) mapping were performed using a FE-SEM 7600F at 20 kV. For S/K ratio analysis, cathode carbon cloth was cleaned with Kimwipes, and catholyte samples were diluted with 30DES, drop-cast on fresh carbon cloth, and dried. Thermogravimetric analysis (TGA) was conducted on the range from 30 to 100 °C with 5 °C min^{-1} on N_2 atmosphere via SDT Q600 TGA. X-ray Photoelectron Spectroscopy (XPS) measurements were conducted using a PHI-5400 spectrometer equipped with a position-sensitive detector (PSD) and an Al Kα X-ray source (250 W). The angle resolution was 45°, and the energy resolution was 0.8 eV. The base pressure of the chamber was maintained at 3.0 × 10^{-7} Pa. All binding energies were calibrated against the C 1s peak at 284.8 eV from adventitious carbon.

Computational Methods: Detailed information is provided in Note S7 (Supporting Information).

Cell Assembly: CR2032 coin cells were used for assembly. The K-BASE disks were purchased from Ionotec Inc. and cut into 15 mm diameter discs. The components were stacked in the following order: negative casing, 0.2 mm SAE-316L stainless steel spacer, wave spring, stainless steel foil, PTFE O-ring, K-BASE disc, PTFE O-ring, carbon cloth, aluminum current collector, 0.2 mm stainless steel spacer, and positive casing. Finally, the assembled cell was compressed at 800 psi using a hydraulic press. The catholyte (52 µL cm^{-2}) was evenly distributed into the carbon cloth, while the K-Na alloy was placed in the stainless steel foil.

Electrochemical Measurements: Galvanostatic cycling tests were conducted using a Neware battery tester (CT-4008Tn-5V50mA-HWX). Electrochemical impedance spectroscopy (EIS) was performed on a Bio-logic SP-150, with a frequency range of 0.01 Hz to 1 MHz and an AC voltage amplitude of 10 mV. Cyclic voltammetry (CV) was conducted over the potential window of 1.5–2.9 V with a scan rate of 0.1 mV s^{-1}. GITT measurements were conducted during discharge (4 M [S]) for 30DES and NiS–30DES cells. Each step consisted of a 30 min discharge at 1.5 mA cm^{-2} (10-min rest) or 0.5 mA cm^{-2} (60-min rest). Linear sweep voltammetry (LSV) using K-Na alloy/BASE/30DES structure was conducted with the voltage range from 1.5 to 2.9 V and 0.5 mV s^{-1} under 60 °C. All electrochemical measurements were carried out in an oven at 60 °C.

Supporting Information

Supporting Information is available from the Wiley Online Library or from the author.

Acknowledgements

L.T. and Q.W. contributed equally to this work. This work was supported by the Singapore Ministry of Education AcRF Tier 2 grant (MOE-T2EP10223-0006). The authors thank the Facility for Analysis, Characterization, Testing, and Simulation (FACTS) in Nanyang Technological University for using the characterization facilities.

Conflict of Interest

The authors declare no conflict of interest.

Data Availability Statement

The data that support the findings of this study are available from the corresponding author upon reasonable request.

Keywords

cycling stability, deep eutectic solvents (DES), intermediate-temperature potassium-sulfur batteries, long-duration energy storage, polysulfide conversion

Received: April 15, 2025
Revised: June 13, 2025
Published online:

[1] O. J. Guerra, *Nat. Energy* **2021**, *6*, 460.
[2] J. A. Dowling, K. Z. Rinaldi, T. H. Ruggles, S. J. Davis, M. Yuan, F. Tong, N. S. Lewis, K. Caldeira, *Joule* **2020**, *4*, 1907.
[3] N. A. Sepulveda, J. D. Jenkins, A. Edington, D. S. Mallapragada, R. K. Lester, *Nat. Energy* **2021**, *6*, 506.
[4] J. D. Jenkins, N. A. Sepulveda, *Joule* **2021**, *5*, 2241.
[5] C. A. Hunter, M. M. Penev, E. P. Reznicek, J. Eichman, N. Rustagi, S. F. Baldwin, *Joule* **2021**, *5*, 2077.

[6] L. Tian, Z. Yang, S. Yuan, T. Milazzo, Q. Cheng, S. Rasool, W. Lei, W. Li, Y. Yang, T. Jin, S. Cong, J. F. Wild, Y. Du, T. Luo, D. Long, Y. Yang, *Nat. Commun.* **2024**, *15*, 7771.
[7] P. Albertus, J. S. Manser, S. Litzelman, *Joule* **2020**, *4*, 21.
[8] M. Staadecker, J. Szinai, P. A. Sánchez-Pérez, S. Kurtz, P. Hidalgo-Gonzalez, *Nat. Commun.* **2024**, *15*, 9501.
[9] F. Yang, S. M. A. Mousavie, T. K. Oh, T. Yang, Y. Lu, C. Farley, R. J. Bodnar, L. Niu, R. Qiao, Z. Li, *Adv. Energy Mater.* **2018**, *8*, 1701991.
[10] Y. Wang, D. Zhou, V. Palomares, D. Shanmukaraj, B. Sun, X. Tang, C. Wang, M. Armand, T. Rojo, G. Wang, *Energy Environ. Sci.* **2020**, *13*, 3848.
[11] X. Xu, D. Zhou, X. Qin, K. Lin, F. Kang, B. Li, D. Shanmukaraj, T. Rojo, M. Armand, G. Wang, *Nat. Commun.* **2018**, *9*, 3870.
[12] Y. Xu, K. Jung, Y.-C. Park, C.-S. Kim, *J. Energy Storage* **2017**, *12*, 215.
[13] K. B. Hueso, M. Armand, T. Rojo, *Energy Environ. Sci.* **2013**, *6*, 734.
[14] Z. Li, C. Wang, F. Ling, L. Wang, R. Bai, Y. Shao, Q. Chen, H. Yuan, Y. Yu, Y. Tan, *Adv. Mater.* **2022**, *34*, 2204214.
[15] A. Y. S. Eng, V. Kumar, Y. Zhang, J. Luo, W. Wang, Y. Sun, W. Li, Z. W. Seh, *Adv. Energy Mater.* **2021**, *11*, 2003493.
[16] J. He, A. Bhargav, L. Su, H. Charalambous, A. Manthiram, *Nat. Commun.* **2023**, *14*, 6568.
[17] G. Nikiforidis, G. J. Jongerden, E. F. Jongerden, M. C. M. van de Sanden, M. N. Tsampas, *J. Electrochem. Soc.* **2019**, *166*, A135.
[18] X. Lu, G. Xia, J. P. Lemmon, Z. Yang, *J. Power Sources* **2010**, *195*, 2431.
[19] W. Bugden, P. Barrow, J. Duncan, *Solid State Ionics* **1981**, *5*, 275.
[20] D. Reed, G. Coffey, E. Mast, N. Canfield, J. Mansurov, X. Lu, V. Sprenkle, *J. Power Sources* **2013**, *227*, 94.
[21] X. Lu, G. Li, J. Y. Kim, D. Mei, J. P. Lemmon, V. L. Sprenkle, J. Liu, *Nat. Commun.* **2014**, *5*, 4578.
[22] X. Lu, G. Li, J. Y. Kim, J. P. Lemmon, V. L. Sprenkle, Z. Yang, *J. Power Sources* **2012**, *215*, 288.
[23] X. Lu, M. E. Bowden, V. L. Sprenkle, J. Liu, *Adv. Mater.* **2015**, *27*, 5915.
[24] I. Yasut, R. Doremus, *J. Am. Ceram. Soc.* **1977**, *60*, 296.
[25] A. Tan, *Solid State Ionics* **1986**, *21*, 67.
[26] O. El Jaroudi, E. Picquenard, N. Gobeltz, A. Demortier, J. Corset, *Inorg. Chem.* **1999**, *38*, 2917.
[27] Q. Cheng, W. Xu, S. Qin, S. Das, T. Jin, A. Li, A. C. Li, B. Qie, P. Yao, H. Zhai, C. Shi, X. Yong, Y. Yang, *Angew. Chem.* **2019**, *131*, 5613.
[28] M. Li, C. Wang, Z. Chen, K. Xu, J. Lu, *Chem. Rev.* **2020**, *120*, 6783.
[29] A. S. Shalygin, E. S. Milovanov, S. S. Yakushkin, O. N. Martyanov, *Pet. Chem.* **2021**, *61*, 1011.
[30] P. Bazylewski, R. Divigalpitiya, G. Fanchini, *RSC Adv.* **2017**, *7*, 2964.
[31] B. T. DiTullio, C. J. Wright, P. Hayes, P. J. Molino, T. W. Hanks, *Colloid Polym. Sci.* **2018**, *296*, 637.
[32] T. Wang, J. He, Z. Zhu, X.-B. Cheng, J. Zhu, B. Lu, Y. Wu, *Adv. Mater.* **2023**, *35*, 2303520.
[33] L. Liu, X. Yin, W. Li, D. Wang, J. Duan, X. Wang, Y. Zhang, D. Peng, Y. Zhang, *Small* **2024**, *20*, 2308564.
[34] J. Zhou, X. Liu, L. Zhu, J. Zhou, Y. Guan, L. Chen, S. Niu, J. Cai, D. Sun, Y. Zhu, J. Du, G. Wang, Y. Qian, *Joule* **2018**, *2*, 2681.
[35] Z. Yan, J. Xiao, W. Lai, L. Wang, F. Gebert, Y. Wang, Q. Gu, H. Liu, S.-L. Chou, H. Liu, S.-X. Dou, *Nat. Commun.* **2019**, *10*, 4793.
[36] C. Zhao, F. Huo, Y. Yang, J. Ruan, F. Chai, H. Xu, Y. Liu, L. Zhang, A. Cabot, Z. Sun, Y. Zhang, *Adv. Funct. Mater.* **2024**, *34*, 2402175.
[37] C. Brady, J. Pan, B. Xu, *Catal. Sci. Technol.* **2020**, *10*, 8429.
[38] J. Ding, H. Zhang, W. Fan, C. Zhong, W. Hu, D. Mitlin, *Adv. Mater.* **2020**, *32*, 1908007.
[39] S. Gu, N. Xiao, F. Wu, Y. Bai, C. Wu, Y. Wu, *ACS Energy Lett.* **2018**, *3*, 2858.
[40] A. Li, S. Kong, C. Guo, H. Ooka, K. Adachi, D. Hashizume, Q. Jiang, H. Han, J. Xiao, R. Nakamura, *Nat. Catal.* **2022**, *5*, 109.
[41] H. S. Pillai, Y. Li, S.-H. Wang, N. Omidvar, Q. Mu, L. E. K. Achenie, F. Abild-Pedersen, J. Yang, G. Wu, H. Xin, *Nat. Commun.* **2023**, *14*, 792.
[42] J. Long, S. Chen, Y. Zhang, C. Guo, X. Fu, D. Deng, J. Xiao, *Angew. Chem.* **2020**, *59*, 9711.
[43] Y. Liu, W. Wang, J. Wang, Y. Zhang, Y. Zhu, Y. Chen, L. Fu, Y. Wu, *Chem. Commun.* **2018**, *54*, 2288.
[44] S. Ma, P. Zuo, H. Zhang, Z. Yu, C. Cui, M. He, G. Yin, *Chem. Commun.* **2019**, *55*, 5267.
[45] J.-Y. Hwang, H. M. Kim, Y.-K. Sun, *J. Mater. Chem. A* **2018**, *6*, 14587.
[46] S. Lee, H. Park, J. Rizell, U.-H. Kim, Y. Liu, X. Xu, S. Xiong, A. Matic, A. T. Zikri, H. Kang, Y.-K. Sun, J. Kim, J.-Y. Hwang, *Adv. Funct. Mater.* **2022**, *32*, 2209145.
[47] X. Zhao, Y. Hong, M. Cheng, S. Wang, L. Zheng, J. Wang, Y. Xu, *J. Mater. Chem. A* **2020**, *8*, 10875.
[48] P. Xiong, X. Han, X. Zhao, P. Bai, Y. Liu, J. Sun, Y. Xu, *ACS Nano* **2019**, *13*, 2536.
[49] Z. Jiang, N. Li, L. Li, F. Tan, J. Huang, S. Huang, *Adv. Mater.* **2024**, *36*, 2311127.
[50] T. Chen, Z. Min, Z. Yu, M. Zheng, Q. Jiang, H. Xu, Y. Sun, K. S. Hui, C. Zha, J. Lu, K. N. Hui, *Adv. Sci.* **2025**, *12*, 2405457.
[51] X. Lu, B. W. Kirby, W. Xu, G. Li, J. Y. Kim, J. P. Lemmon, V. L. Sprenkle, Z. Yang, *Energy Environ. Sci.* **2013**, *6*, 299.
[52] W. Song, X. Yang, T. Zhang, Z. Huang, H. Wang, J. Sun, Y. Xu, J. Ding, W. Hu, *Nat. Commun.* **2024**, *15*, 1005.
[53] C. Ye, J. Shan, D. Chao, P. Liang, Y. Jiao, J. Hao, Q. Gu, K. Davey, H. Wang, S.-Z. Qiao, *J. Am. Chem. Soc.* **2021**, *143*, 16902.
[54] N.-C. Lai, G. Cong, Y.-C. Lu, *J. Mater. Chem. A* **2019**, *7*, 20584.
[55] C. Ye, J. Shan, H. Li, C.-C. Kao, Q. Gu, S.-Z. Qiao, *Angew. Chem.* **2023**, *135*, 202301681.
[56] X. Ge, H. Di, P. Wang, X. Miao, P. Zhang, H. Wang, J. Ma, L. Yin, *ACS Nano* **2020**, *14*, 16022.
[57] S. Zhang, Y. Kong, Y. Gu, R. Bai, M. Li, S. Zhao, M. Ma, Z. Li, L. Zeng, D. Qiu, Q. Zhang, M. Luo, L. Gu, Y. Yu, S. Guo, J. Zhang, *J. Am. Chem. Soc.* **2024**, *146*, 4433.
[58] H. Liang, P. Kumar, Z. Ma, F. Zhao, H. Cheng, H. Xie, Z. Cao, L. Cavallo, Q. Li, J. Ming, *ACS Energy Lett.* **2024**, *9*, 3536.
[59] S. Ye, N. Yao, X. Chen, M. Ma, L. Wang, Z. Chen, Y. Yao, Q. Zhang, Y. Yu, *Angew. Chem.* **2023**, *135*, 202307728.
[60] J. Liang, W. Song, H. Wang, J. Ding, W. Hu, *Nanomaterials* **2022**, *12*, 3968.
[61] V. K. Bharti, A. D. Pathak, A. Anjan, C. S. Sharma, M. Khandelwal, *ACS Sustainable Chem. Eng.* **2022**, *10*, 16634.
[62] L. Hu, X. Meng, L. Liu, D. Liang, S. Liang, L.-L. Wang, L. Yang, T. Ding, C. Deng, Q. Dong, *Chem. Commun.* **2021**, *57*, 1490.
[63] K. Yang, S. Kim, X. Yang, M. Cho, Y. Lee, *Small Methods* **2022**, *6*, 2100899.
[64] K. Yang, J. Chen, S. Kim, P. Xiong, W. Chen, M. Cho, Y. Lee, *ACS Energy Lett.* **2023**, *8*, 2169.
[65] M. M. Li, X. Lu, X. Zhan, M. H. Engelhard, J. F. Bonnett, E. Polikarpov, K. Jung, D. M. Reed, V. L. Sprenkle, G. Li, *Chem. Commun.* **2021**, *57*, 45.
[66] R. M. Darling, K. G. Gallagher, J. A. Kowalski, S. Ha, F. R. Brushett, *Energy Environ. Sci.* **2014**, *7*, 3459.
[67] O. Schmidt, S. Melchior, A. Hawkes, I. Staffell, *Joule* **2019**, *3*, 81.